Highly Nonstoichiometric YAG Ceramics with Modified Luminescence Properties

Weiwei Cao[1], Ana Isabel Becerro[2], Victor Castaing[2], Xue Fang[1], Pierre Florian[1], Franck Fayon[1], Didier Zanghi[1], Emmanuel Veron[1], Alessio Zandonà[1], Cécile Genevois[1], Michael J. Pitcher[1] and Mathieu Allix[1]**

[1] CNRS, CEMHTI UPR3079, 1d Avenue de la Recherche Scientifique, 45071 Orléans, France

[2] Instituto de Ciencia de Materiales de Sevilla (CSIC-US), c/Américo Vespucio, 49, 41092 Seville, Spain

Email: michael.pitcher@cnrs-orleans.fr, mathieu.allix@cnrs-orleans.fr

Keywords: (YAG, aerodynamic levitation, nonstoichiometry, luminescence)

Abstract

$Y_3Al_5O_{12}$ (YAG) is a widely used phosphor host. Its optical properties are controlled by chemical substitution at its YO_8 or AlO_6/AlO_4 crystallographic sublattices, with emission wavelengths defined by rare-earth (for YO_8) and transition-metal (for AlO_6/AlO_4) dopants which have been explored extensively. Nonstoichiometric compositions $Y_{3+x}Al_{5-x}O_{12}$ ($x \neq 0$) may offer a route to new emission wavelengths by distributing dopants over both crystallographic sublattice types, but deviation from $Y_3Al_5O_{12}$ stoichiometry is difficult to achieve and limited generally to $0 < x < 0.03$. Here, a series of highly nonstoichiometric $Y_{3+x}Al_{5-x}O_{12}$ is reported with $0 \leq x \leq 0.40$, corresponding to ≤ 20% of the AlO_6 sublattice substituted by Y^{3+}, synthesised by advanced melt-quenching techniques. This impacts the up-conversion luminescence of Yb^{3+}/Er^{3+}-doped systems, whose yellow-green emission differs from the red-orange emission of their stoichiometric counterparts. In contrast, the larger Ce^{3+} ion in nonstoichiometric YAG:Ce^{3+} occupies the YO_8 sublattice exclusively, and its down-conversion emission is hardly affected. Analogous highly nonstoichiometric systems should be obtainable for a range of functional garnets, demonstrated here by the synthesis of $Gd_{3.2}Al_{4.8}O_{12}$ and $Gd_{3.2}Ga_{4.8}O_{12}$. This opens the way to property tuning by control of garnet host stoichiometry, and the prospect of improved performance or new applications for garnet-type materials.

Introduction

Yttrium aluminium garnet $Y_3Al_5O_{12}$ (YAG) is a widely used phosphor host material with notable commercial and technological applications in white LED lighting[1], scintillation detectors[2] and solid state lasers.[3] Its crystal structure, of general formula $A_3B_2C_3O_{12}$, contains three Y^{3+} cations per formula unit exclusively in 8-fold dodecahedral coordination by oxide at the A site (YO_8), with five Al^{3+} cations distributed between the octahedral B site (AlO_6) and tetrahedral C site (AlO_4). This provides chemical versatility, as the A (Y^{3+}) site can accommodate rare earth (RE^{3+}) dopants with a range of ionic radii spanning most of the lanthanide series, whilst the B and C (Al^{3+}) sites may be substituted by other transition- and post-transition metals, producing a range of characteristic emission bands that underpin its applications. This versatility can lead to relatively complex systems such as $Y_3Al_2Ga_3O_{12}$, where Ce^{3+} and Cr^{3+} can be co-substituted with tuning of the Al^{3+}/Ga^{3+} ratio to generate high performance persistent phosphors.[4,5] Whilst A, B and C sites can host many different substituents, the structure is far less tolerant of deviations from $A_3B_2C_3O_{12}$ stoichiometry, to the extent that YAG is often considered as an archetypal line phase. Nevertheless, off-stoichiometric (as opposed to highly nonstoichiometric) Y-rich single crystals have been reported by melt-growth of aluminate and gallate garnets,[6–8] with the presence of ≤ 1 at.% excess Y^{3+} at the Al^{3+} sublattice inferred spectroscopically,[7,8] consistent with theoretical studies that identify the B site as the most energetically favourable Y^{3+} defect host.[9,10] Similarly, off-stoichiometric ceramics have been reported with up to 1 at.% Y^{3+} excess (*i.e.* $Y_{3.03}Al_{4.97}O_{12}$) deduced from systematic analysis of lattice parameters,[11] but such a limited stability range makes it challenging to synthesise and characterise these materials.[12]

The near-total segregation of the [A] and [B/C] cations into their respective [8-] and [6/4]-coordinate sites means that RE^{3+} dopants into YAG adopt 8-fold coordination, producing predictable and well-characterised luminescence properties. In principle, the disruption of $[A_3][B_2C_3]O_{12}$ stoichiometry by increasing the $[A_3]/[B_2C_3]$ ratio (*i.e.* $Y_{3+x}Al_{5-x}O_{12}$ with $x >> 0$) could offer a way to modify the wellestablished visible emission spectra of doped YAGs, if the additional crystallographic sites occupied by excess Y^{3+} can themselves be populated with significant quantities of RE^{3+} emission centres: thus activator ions could be distributed over both cubic and octahedral (or tetrahedral) coordination geometries, with substantial local perturbations at each site due to different nearest- and next-nearest neighbour configurations. Such highly nonstoichiometric materials have not been realised by conventional high temperature crystal-growth or ceramic syntheses, but may be accessible by low temperature or non-equilibrium routes that promote metastable phase formation. Indeed, a solution-based route to Y-rich YAG scintillators has been attempted with limited success.[13] More concretely, in stoichiometric systems, non-typical YAG compositions have been demonstrated to form under conditions where phase formation occurs at relatively low temperatures, for example using solvothermal methods to access extremely high Ce^{3+} concentrations in YAG:Ce nanopowders.[14] Similarly, melt-quenching techniques offer non-equilibrium routes to a range of metastable aluminates and gallates with similar chemistries to YAG, by crystallisation at temperatures below those typically required for solid-state reactions.[15–18]

Glassy YAG materials can be synthesised by containerless melt-quenching approaches including aerodynamic levitation[19] and spray pyrolysis methods,[20,21] and these crystallise into the cubic garnet structure at approximately 900°C, far below the range 1600-1700°C typically required for ceramic synthesis of YAG.[22] Laser melting of aerodynamically-levitated samples is useful in this context as it offers access to temperatures that are high enough to melt YAG, whilst the absence of a container-melt interface inhibits heterogeneous crystallisation on cooling, allowing access to non-equilibrium states (*i.e.* glass or deeply-undercooled melts)[23] from which crystallisation occurs. In the Y_2O_3-Al_2O_3 phase field, the glass-crystallisation approach has facilitated the synthesis of transparent alumina-rich YAG-Al_2O_3 nanoceramics,[24] and aerodynamic levitation has also been applied to study crystallisation dynamics[25,26] and phase separation[27,28] of melts with compositions close to $Y_3Al_5O_{12}$. Intriguingly, results presented in the earliest of these studies[25] suggested the potential to stabilise highly nonstoichiometric yttrium-rich garnets by glass crystallisation, but these were not developed further. Here we report the synthesis of highly nonstoichiometric $Y_{3+x}Al_{5-x}O_{12}$ with $0 \leq x \leq 0.40$ by crystallisation of their undercooled melts or glasses, their crystal structures, and the doping of these materials with the RE^{3+} phosphors Ce^{3+} and Yb^{3+}/Er^{3+} whose contrasting ionic radii produce different crystallographic coordination preferences. The responses of their optical emission properties may open pathways to new or improved applications for this important class of materials.

Results and Discussion

Synthesis and structure of nonstoichiometric YAG. A provisional series $Y_{3+x}Al_{5-x}O_{12}$ was prepared in the nominal range $0 \leq x \leq 0.30$ by laser melting of pelletised reaction mixtures, which were levitated aerodynamically in an argon gas jet, followed by free cooling of the levitating melts by switching off the lasers (see **Methods**). All of these melts exhibited recalescence on cooling, indicative of crystallisation. PXRD analysis of crushed beads indicated two types of crystallisation behaviour: (i) crystallisation into a garnet (YAG-type) structure as the only crystalline phase, and (ii) crystallisation into multiple phases, dominated by perovskite ($YAlO_3$) and corundum (Al_2O_3). The garnet (YAG-type) samples exhibited large, systematic shifts of the Bragg peaks towards low 2Θ angles for compositions $x > 0$, implying the formation of a solid solution of type $Y_{3+x}Al_{5-x}O_{12}$ (see **Figure S1**). However, examples of both crystallisation behaviours were obtained from all compositions, highlighting the need to better control the synthesis conditions to obtain phase-pure $Y_{3+x}Al_{5-x}O_{12}$ garnets reliably.

To do this, the effect of cooling rate on the crystallisation behaviour of a representative composition $Y_{3.2}Al_{4.8}O_{12}$ ($x = 0.20$) was measured systematically, using the bead mass to control the radiative cooling rates of 36 samples. This revealed a close correlation between cooling rate, crystallisation temperature, and the crystalline phases obtained, as shown in **Figure 1**. The slowest cooling rates of < 400 °C s^{-1} (averaged over the temperature interval 2100 – 1300 °C) led to crystallisation of the melt at 1200 – 1300 °C, yielding a mixture of perovskite ($YAlO_3$) and corundum (Al_2O_3). Intermediate cooling rates of 400 – 550 °C s^{-1} resulted in lower crystallisation temperatures of 900 – 1000°C, and produced single-phase garnet-type samples. The highest cooling rates of > 550 °C s^{-1} did not exhibit recalescence, and yielded near-transparent glassy materials. These glassy beads are predominantly amorphous with a small population of YAG-type microcrystals and a thin (≤ 5 μm) crystallised surface layer (see **Supplementary Information, Section A**). They can be crystallised fully, leaving no apparent residual glass, using a single heating step of 1000 °C for 2 hours to produce a single-phase garnet of composition $Y_{3.2}Al_{4.8}O_{12}$ (an example of this process is shown in **Figure S2**). Despite the optical isotropy of the cubic YAG crystals, only opaque beads were obtained due to the presence of porosity

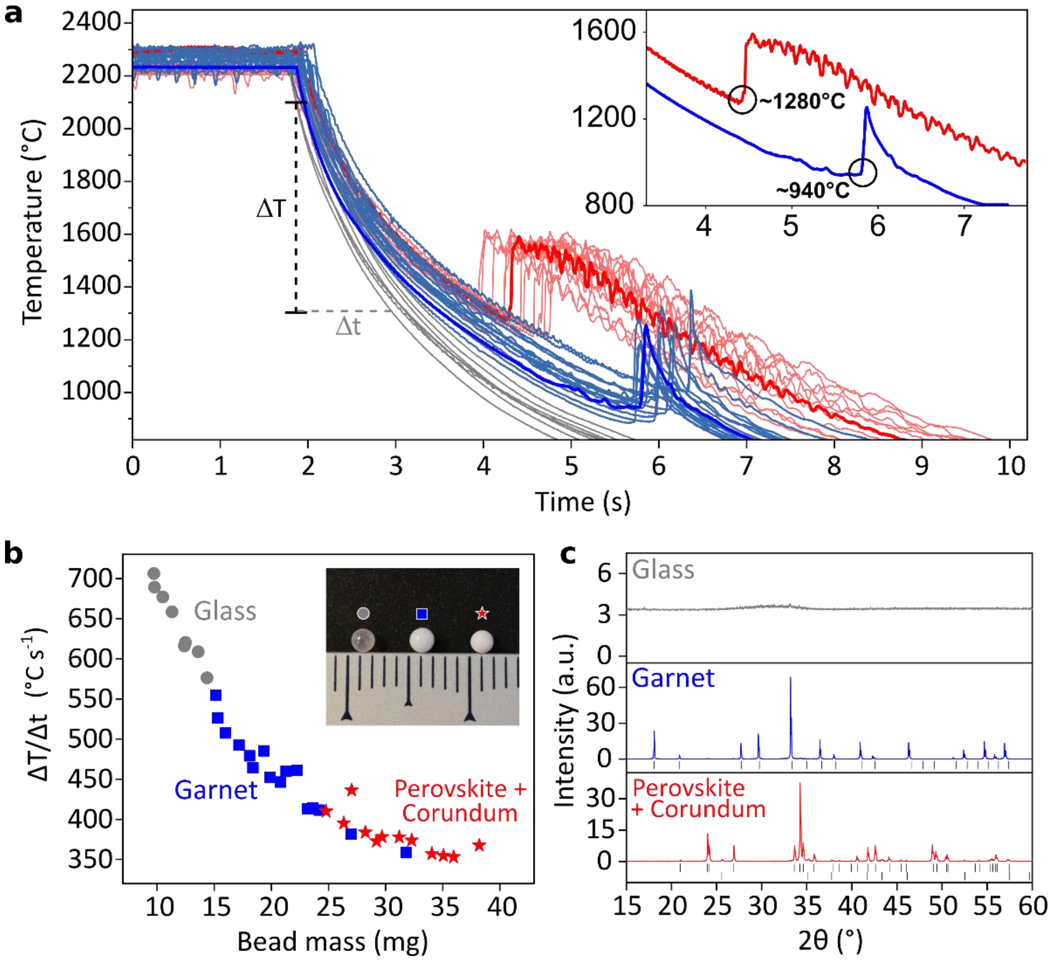

Figure 1. Synthesis of garnet-type $Y_{3.2}Al_{4.8}O_{12}$ (x = 0.2) by melt-quenching. (a) Cooling curves recorded in-situ for 36 quenched melts, colour coded to show melts that formed glass (grey), garnet (blue) and mixed phase perovskite/corundum (red). The inset shows a direct comparison between typical garnet-forming (blue) and perovskite/corundum forming (red) crystallisation events. (b) Cooling rates, defined as the time taken (Δt, variable) to cool through the region 2100 – 1300°C (ΔT, fixed), as a function of bead mass, and the corresponding reaction products from each quench. The inset shows a photograph of the three different bead types obtained. (c) Representative PXRD patterns (Cu K_{α}) of the resulting glass, garnet and perovskite/corundum samples.

(**Figure S2**). Nonstoichiometric YAGs can therefore be obtained from the melt, either by direct crystallisation or indirectly by crystallisation of a quenched glass, if the melt can be cooled from 2200 – 900°C in 4 seconds or less.

Both of these routes were used together to synthesise a solid solution in the range $0 \leq x \leq 0.40$. Single-phase $Y_{3+x}Al_{5-x}O_{12}$ samples with $0 \leq x \leq 0.29$ were isolated conveniently by one-step direct crystallisation of the melt in an argon jet, but single-phase samples with $x \geq 0.30$ could not be obtained in this way. For compositions $0.30 \leq x \leq 0.40$, precursor glasses were obtained by using smaller beads and an oxygen gas jet to achieve consistently high cooling rates >550 °C s^{-1} (see **Figure S3**), and these were pulverised and crystallised at 1000°C for 2h in a second step to yield single-phase YAGs by glass-crystallisation. Outside of this range, we found no evidence for the formation of Al-rich "$Y_{2.9}Al_{5.1}O_{12}$" ($x = -0.10$), consistent with the tendency of such melts to phase separate,[24] whilst compositions $x > 0.40$ produced mixtures $YAlO_3$ and Al_2O_3 with stoichiometric YAG as a minority phase (see **Figure S4**). The as-synthesised nonstoichiometric YAGs have a high thermal stability, as shown by in-situ PXRD of $Y_{3.4}Al_{4.6}O_{12}$ ($x = 0.40$) on heating, which reveals a decomposition to stoichiometric $Y_3Al_5O_{12}$, $YAlO_3$ and $Y_4Al_2O_9$ at ~1350 °C (**Figure S5**).

Figure 2 shows the structural evolution of the series $0 \leq x \leq 0.40$ as investigated by Rietveld analysis of synchrotron X-ray powder diffraction (SXRD) data (see **Supplementary Information Section B** for refinement protocols, fits and tabulated structures). These refinements produced clear structural trends as a function of x, with a strong linear increase in unit cell volume in the range $0 \leq x \leq 0.40$, consistent with the formation of a solid solution (**Figure 2c**). For each composition, the excess Y^{3+} was found to occupy the *B* site (Wyckoff symbol 16*a*), with no detectable Y^{3+} occupancy at the *C* sites (24*d*). This is reflected in the response of the refined *M*-O distances at each site: Al_{16a}-O shows a pronounced increase with x due to Y^{3+} substitution, whilst Al_{24d}-O remains almost constant across the series as the 24*d* site is occupied only by Al^{3+} (**Figure 2d**). Thus, the compositions can be reformulated as $Y_3\,[Al^{VI}_{2-x}Y_x][Al^{IV}]_3O_{12}$, with x = 0.40 corresponding to substitution of 20% of the *B* sites by Y^{3+}.

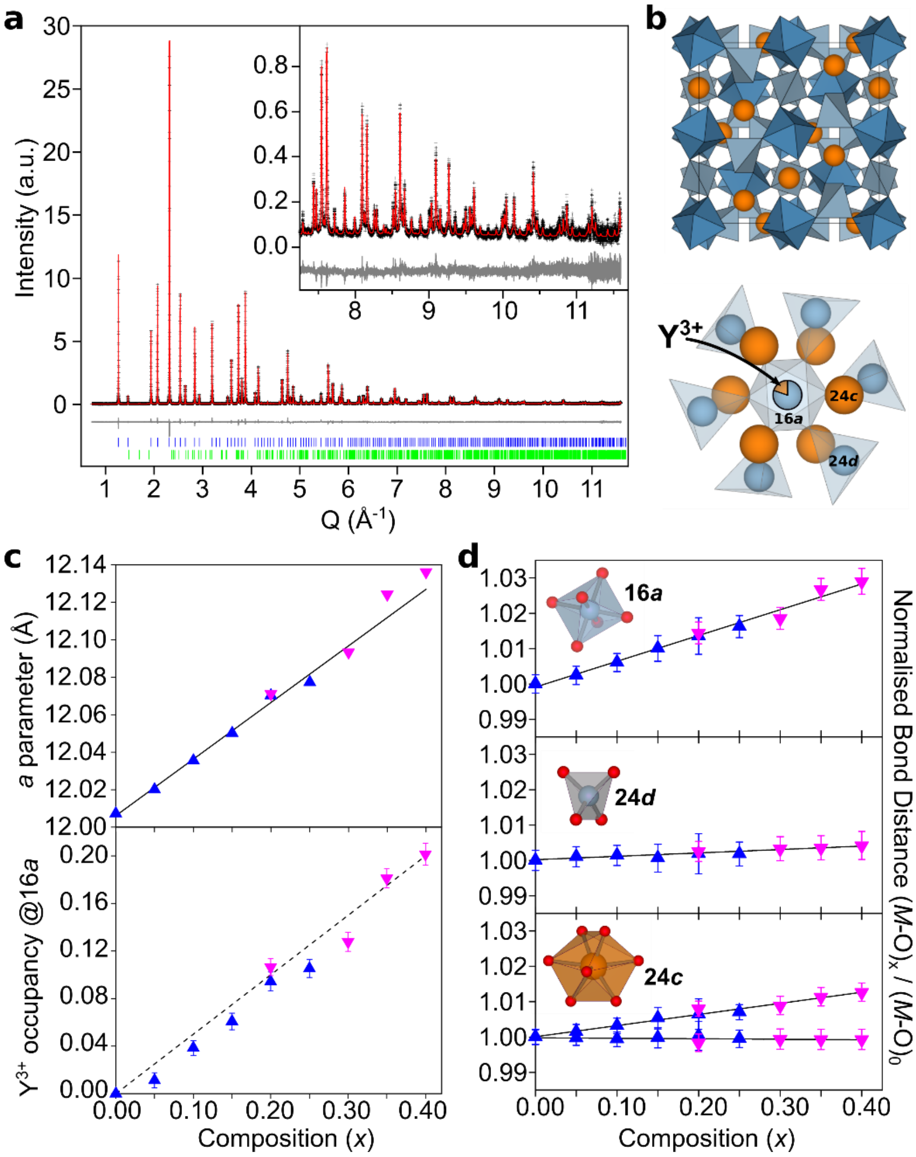

Figure 2. Structural evolution of $Y_{3+x}Al_{5-x}O_{12}$ ($0 \le x \le 0.4$) from Rietveld analysis of SXRD data. (a) Rietveld refinement of $Y_{3.4}Al_{4.6}O_{12}$ (R_{wp} = 8.79%, χ = 1.16) with zoom of the high angle fit inset. Blue tick marks indicate garnet reflections (99.77(2) wt.%), green tick marks indicate perovskite reflections ($YAlO_3$, 0.33(2) wt.%) (b) The garnet structure of $Y_{3.4}Al_{4.6}O_{12}$ projected along (100), and a fragment projected along (111) showing the three different cation environments (orange atoms = Y^{3+}; dark blue octahedra = AlO_6; light blue tetrahedra = AlO_4). (c) Refined lattice parameter *a* with linear fit overlaid (solid line), and refined occupancy of the 16*a* site by Y^{3+} with nominal occupancy overlaid (dashed line). (d) Refined metal-oxygen distances $(M\text{-}O)_x$ in the three different cation environments, normalised to their values at $Y_3Al_5O_{12}$ $(M\text{-}O)_0$. Blue triangles = direct crystallised samples; magenta inverted triangles = glass crystallised samples. Error bars correspond to 10x esd from the refinements.

To complement the Rietveld-obtained average structures, TEM, and $^{89}Y/^{27}Al$ MAS-NMR and EXAFS spectroscopies were used independently to characterise octahedral Y^{3+} at the nanometric and local atomic scales. Atomic resolution STEM-HAADF images of very thin specimens of composition x = 0, 0.20 and 0.40 prepared by ion beam milling (respective thicknesses 13.5, 8.0 and 14.5 nm measured by EELS, equivalent to 7 – 12 unit cells), oriented along [001], revealed random increases of intensity of the 16*a* columns (*B* site) as the material becomes nonstoichiometric (**Figure 3a – e**, and **Supplementary Information Section C**). Such excess intensity is expected from the substitution of Al (*Z* = 13) for Y (*Z* = 39) in the 16*a* columns, and this is confirmed directly by spectroscopic observation of Y in these columns by EDS mapping (**Figure 3g, h**). Similarly, the randomness of intensity is consistent with different discrete numbers of Y^{3+} atoms hosted by each 16*a* column, visible here due to the extreme sample thinness. The STEM-HAADF intensity profiles of $Y_{3.4}Al_{4.6}O_{12}$ were used to calculate the number of Y^{3+} ions per 16*a* column. The resulting histogram (bars in **Figure 3f**) corresponds closely to a statistically random arrangement plotted as a normal distribution (line in **Figure 3f**). These results are consistent with the crystallographic location of excess Y^{3+} at 16*a*, distributed randomly at the nanoscale, with no indication of clustering.

To support the analysis of local structural response to the incorporation of excess Y^{3+}, expected $^{89}Y/^{27}Al$-NMR and Y *K*-edge EXAFS parameters were calculated from ensembles of DFT-relaxed model structures with x = 0, 0.125, 0.25 and 0.325, constructed from single unit cells (1 x 1 x 1) by substitution of 1, 2 or 3 *B* sites by Y^{3+} (see **Methods** and **Figure S6**). The experimental ^{89}Y MAS-NMR spectra feature a single resonance at 220 ppm corresponding to a single YO_8 environment when x = 0. The spectra of x = 0.10, 0.20, 0.30 and 0.40 contain an additional resonance of increasing intensity at 400-420 ppm, which corresponds to the calculated chemical shift range for a YO_6 environment (**Figure 4a**). In parallel, the YO_8 resonance shows a systematic upfield shift with x and splits into multiple components due to the presence of 0, 1, or 2 YO_6 near-neighbours (**Figure 4b**). The relative fitted intensities of the YO_8 and YO_6 components are consistent with the ratios expected from the nominal sample compositions. Furthermore, the chemical shifts of the individual YO_8

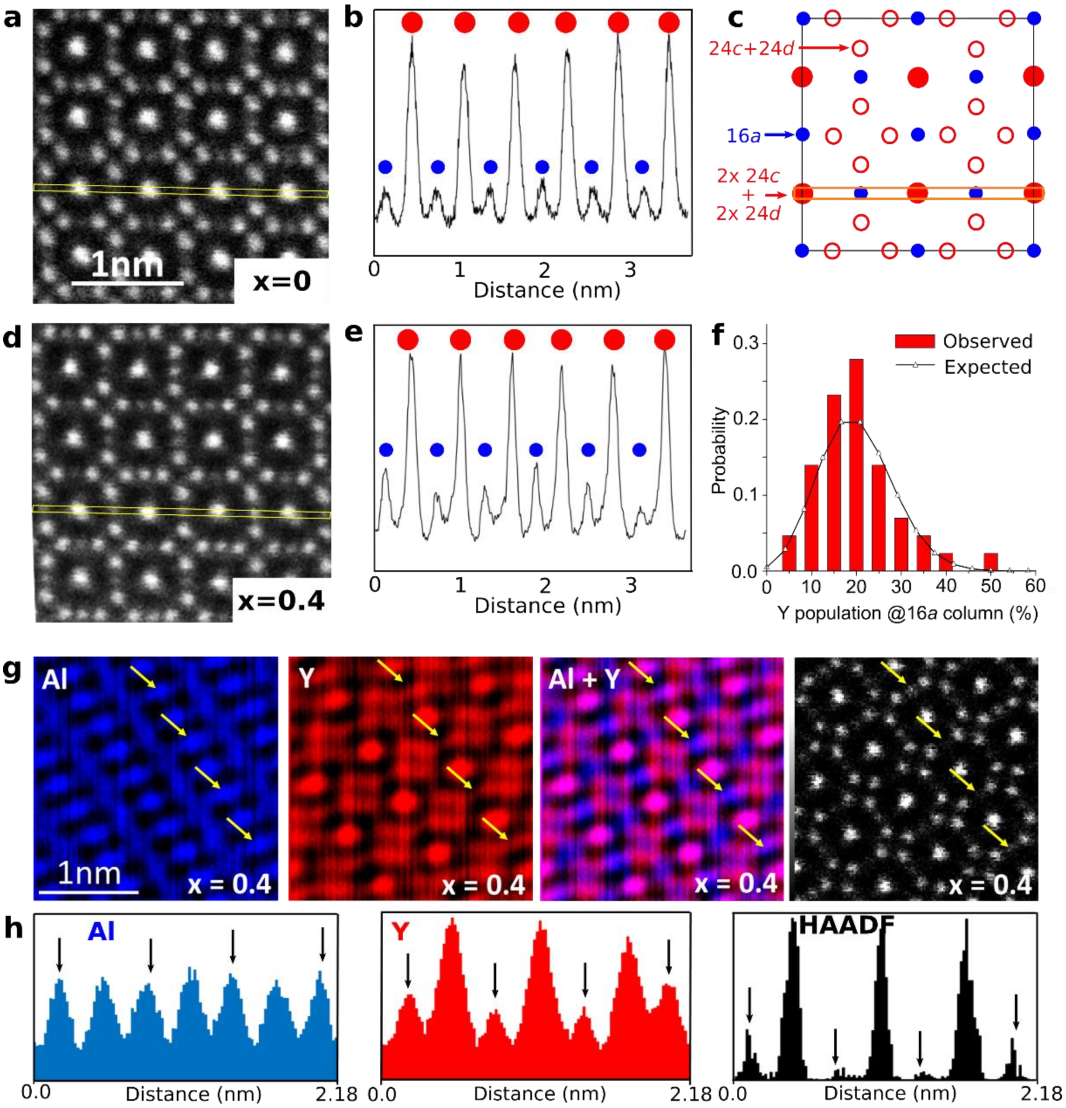

Figure 3. Atomic resolution STEM-HAADF and STEM-EDS analysis of $Y_3Al_5O_{12}$ (x = 0) and $Y_{3.4}Al_{4.6}O_{12}$ (x = 0.40) oriented along [100]. (a) STEM-HAADF image of $Y_3Al_5O_{12}$ with analysed strip indicated by the yellow box, (b) extracted intensity profile, (c) unit cell projection [100] labelled with atomic columns and a box representing the analysed strip. (d, e) The corresponding STEM-HAADF image and extracted intensity profile for $Y_{3.4}Al_{4.6}O_{12}$. (f) For x = 0.4, observed distribution of Y^{3+} in the 16*a* columns from STEM-HAADF fitted intensity profiles (red bars), overlaid with the expected trend from a random distribution of Y atoms within the 16*a* columns, calculated as a normal distribution (black line). (g) For x = 0.40, atomic resolution EDS maps of Al (blue), Y (red) and combined (Al+Y), and the corresponding STEM-HAADF image. (h) intensity profiles of STEM-EDS (Al, Y) and STEM-HAADF with arrows to indicate the A1 sites. The arrows in (g) and (h) indicate the same profiled 16*a* sites.

components agree closely with GIPAW-calculated values from the DFT-relaxed models, and their relative intensities are consistent with a structural model with a random distribution of Y^{3+} at the 16*a* sites at the unit cell length scale (see **Supplementary Information Section D** for further discussion and tabulated data). Similarly, the ^{27}Al line profiles evolve continuously with increasing non-stoichiometry, with additional components apparent in the AlO_4 and AlO_6 resonances in agreement with the nominal compositions and a random YO_6 distribution (see **Supplementary Information section D**). EXAFS analysis complements these observations by highlighting the local structural perturbation caused by larger Y^{3+} ions at the 16*a* sites: these spectra show a pronounced evolution with x (**Figure S7**), which agrees qualitatively with theoretical spectra from the DFT models (where Y_{16a}-O ≈ 2.18 Å locally), but matches poorly to theoretical spectra from the Rietveld models, where the M_{16a}-O distance is averaged to ~1.96 Å and hence underestimated for Y (see **Supplementary Information Section E**). At the same time, the extracted monotonic decrease of $R_{Y\text{-}O}$ (the average Y-O distance, **Figure S7**) is consistent with an increasing proportion of YO_6 sites. These techniques confirm the presence of the excess Y^{3+} within the garnet structure at the B (16*a*) site, and taken together with the STEM-HAADF data, indicate that octahedral Y^{3+} sites are arranged randomly in these materials.

Structure and luminescence of doped ns-YAGs. Two physically contrasting dopant systems were selected to test the effect of non-stoichiometry on the luminescence properties: a singly-doped system with 5% Ce^{3+} for down-conversion[29], and a co-doped system with 20% Yb^{3+}/2% Er^{3+} for up-conversion[30]. A non-stoichiometry of $x = 0.20$ was selected for both systems, due to its high concentration of Y^{3+} at the 16*a* site (10%), ease of synthesis, and sufficient distance from the solid solution limit. To minimise potential differences linked to processing conditions, such as anti-site defect formation, the samples were all prepared by the same method (direct crystallisation of the melt) and the beads were crushed into powders prior to measurement. Rietveld refinements revealed contrasting dopant site preferences in the two systems (see **Supplementary Information Section B** for refinements and tabulated structures). In $(Y_{0.95}Ce_{0.05})_{3.2}Al_{4.8}O_{12}$, Ce^{3+} was found to occupy the 24*c* site exclusively (0.949(4) Y^{3+} / 0.051(4) Ce^{3+}) with no detectable amount at the 16*a* site. In $(Y_{0.78}Yb_{0.2}Er_{0.02})_{3.2}Al_{4.8}O_{12}$, Yb(Er)$^{3+}$ shows a strong preference for octahedral coordination, out-competing Y^{3+} for the 16*a* site, which has a refined composition 0.90 Al^{3+} / 0.0155(6) Y^{3+} / 0.0846(5) Yb(Er)$^{3+}$. The remainder occupy the 24*c* site (MO_8), of refined composition 0.8217(4) Y^{3+} / 0.1783(3) Yb(Er)$^{3+}$.

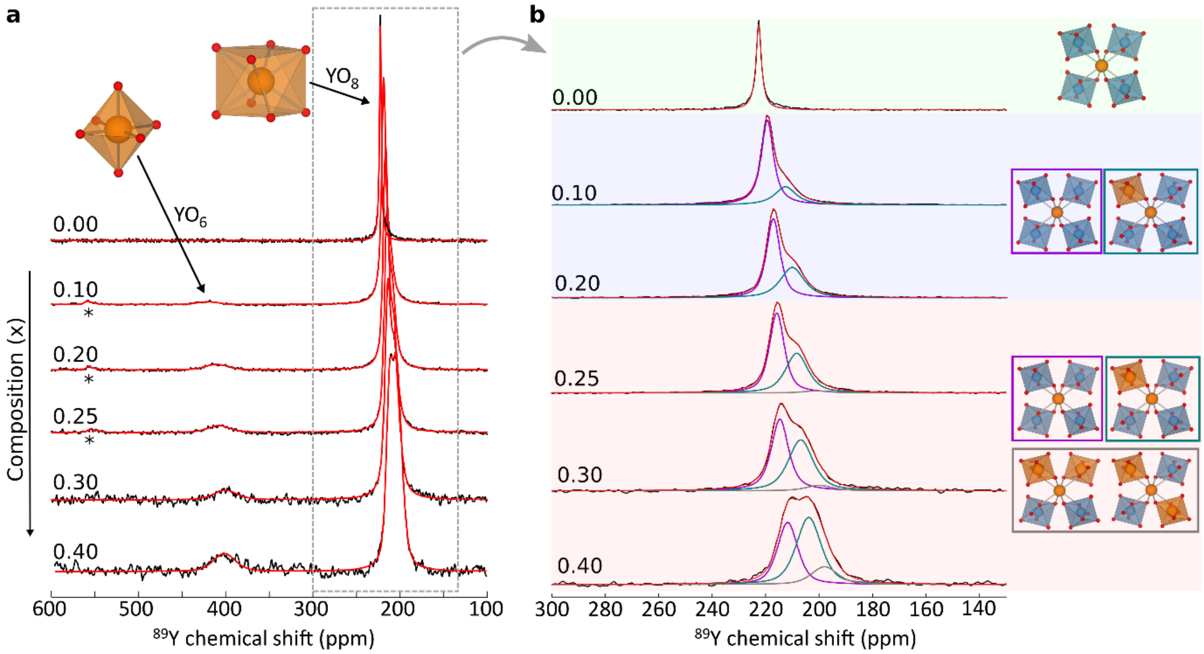

Figure 4. Local structural response to Y^{3+} substitution at the 16*a* site in $Y_{3+x}Al_{5-x}O_{12}$. (a) ^{89}Y NMR spectra showing the emergence of a new resonance above 400 ppm due to YO_6, whose intensity increases with *x*. This induces additional components in the YO_8 resonance at 220 ppm from the presence of zero, one or two YO_6 units in its nearest-neighbour sphere, as illustrated in panel (b), where black line = data, red line = overall fit, violet component = zero YO_6 neighbours, green component = one YO_6, grey component = two YO_6. All samples are doped with 0.1 mol% Gd^{3+} to reduce ^{89}Y longitudinal relaxation time (see **Methods**). Asterisks (*) indicate spinning side bands.

The emission spectra of stoichiometric $(Y_{0.95}Ce_{0.05})_3Al_5O_{12}$ and nonstoichiometric $(Y_{0.95}Ce_{0.05})_{3.2}Al_{4.8}O_{12}$, which both accommodate Ce^{3+} at the 24*c* site, are near-identical (**Figure 5f**). In contrast, non-stoichiometry has a strong influence on the emission spectra of the Yb/Er doped YAG. **Figure 5a-d** shows the up-conversion (UC) emission spectra of stoichiometric $(Y_{0.78}Yb_{0.2}Er_{0.02})_3Al_5O_{12}$ and nonstoichiometric $(Y_{0.78}Yb_{0.2}Er_{0.02})_{3.2}Al_{4.8}O_{12}$ recorded under 980 nm laser excitation. The spectrum of

$(Y_{0.78}Yb_{0.2}Er_{0.02})_3Al_5O_{12}$ agrees well with the published UC emission spectra of Yb/Er-doped YAG[31–34], with two emission bands located at 520 – 570 nm (green emission) and 640 – 700 nm (red emission), corresponding to the $^4S_{3/2}$, $^2H_{11/2} \rightarrow {}^4I_{15/2}$ and $^4F_{9/2} \rightarrow {}^4I_{15/2}$ Er^{3+} transitions, respectively. The spectrum of $(Y_{0.78}Yb_{0.2}Er_{0.02})_{3.2}Al_{4.8}O_{12}$ also consists of two emission bands located in the green and red regions, although their fine structure has changed significantly: the most intense peak of the red band now occurs at 663 nm, coinciding with the lowest intensity peak in the red band of the stoichiometric material. Likewise, the most intense peak in the green band of x = 0.2 occurs at 546 nm, instead of 555 nm. The emission colour of both samples is therefore different, as plotted in the CIE chromaticity diagram in **Figure 5e**. To the naked eye, stoichiometric $(Y_{0.78}Yb_{0.2}Er_{0.02})_3Al_5O_{12}$ emits a red-orange light, but the light emitted by nonstoichiometric $(Y_{0.78}Yb_{0.2}Er_{0.02})_{3.2}Al_{4.8}O_{12}$ appears green (see inset of **Figure 5e**). Repeated measurements on different powder samples revealed consistent red-orange emission for stoichiometric $(Y_{0.78}Yb_{0.2}Er_{0.02})_3Al_5O_{12}$ samples, whilst nonstoichiometric $(Y_{0.78}Yb_{0.2}Er_{0.02})_{3.2}Al_{4.8}O_{12}$ samples were all strongly green-shifted with some sample-dependent variation. Measurements on polished disks of $(Y_{0.78}Yb_{0.2}Er_{0.02})_3Al_5O_{12}$, $(Y_{0.78}Yb_{0.2}Er_{0.02})_{3.1}Al_{4.9}O_{12}$ and $(Y_{0.78}Yb_{0.2}Er_{0.02})_{3.2}Al_{4.8}O_{12}$ (x = 0, 0.10, 0.20), fabricated by polishing single directly-crystallised beads, revealed similar behaviour: a progressive shift towards green emission with increasing x, with some sample-dependent variation within the nonstoichiometric samples (see **Supporting Information Section F**). The colour shift with increasing x is associated with an increasing population of $(Yb/Er)O_6$ sites coupled to a proliferation of locally-inequivalent A sites (as shown earlier, **Figure 4b**). Although these materials appear to be compositionally homogeneous (see electron microprobe measurements, **Supporting Information Section G**), this implies the presence of subtle differences in Y^{3+}, Yb^{3+} and Er^{3+} (16*a*) distribution, which may be highly sensitive to the precise crystallisation conditions.

The trend in up-conversion intensities of the green and red emission bands as a function of pumping power indicate a two-photon absorption process in agreement with the literature on Yb/Er-doped YAGs,[35,36] indicating that non-stoichiometry does not alter the main UC mechanism (see **Supporting**

Information Section F). The luminescence decay curves of both red and green emissions of the stoichiometric sample (**Figure 5b**) fitted well to a single exponential decay of the form $I(t) = I \exp(-t/\tau)$, producing single lifetime values (τ) of 426 μs and 206 μs respectively. In contrast, for the nonstoichiometric sample, the decay curves (**Figure 5d**) required a biexponential function of form $I(t) = I_1 \exp(-t/\tau_1) + I_2 \exp(-t/\tau_2)$ to ensure a good fit. This revealed a long-lifetime component (411 and 158 μs), in addition to a short-lifetime component (128 and 62 μs) which is larger for both transitions (62% and 63% of the total intensity, respectively). The fitting parameters from both

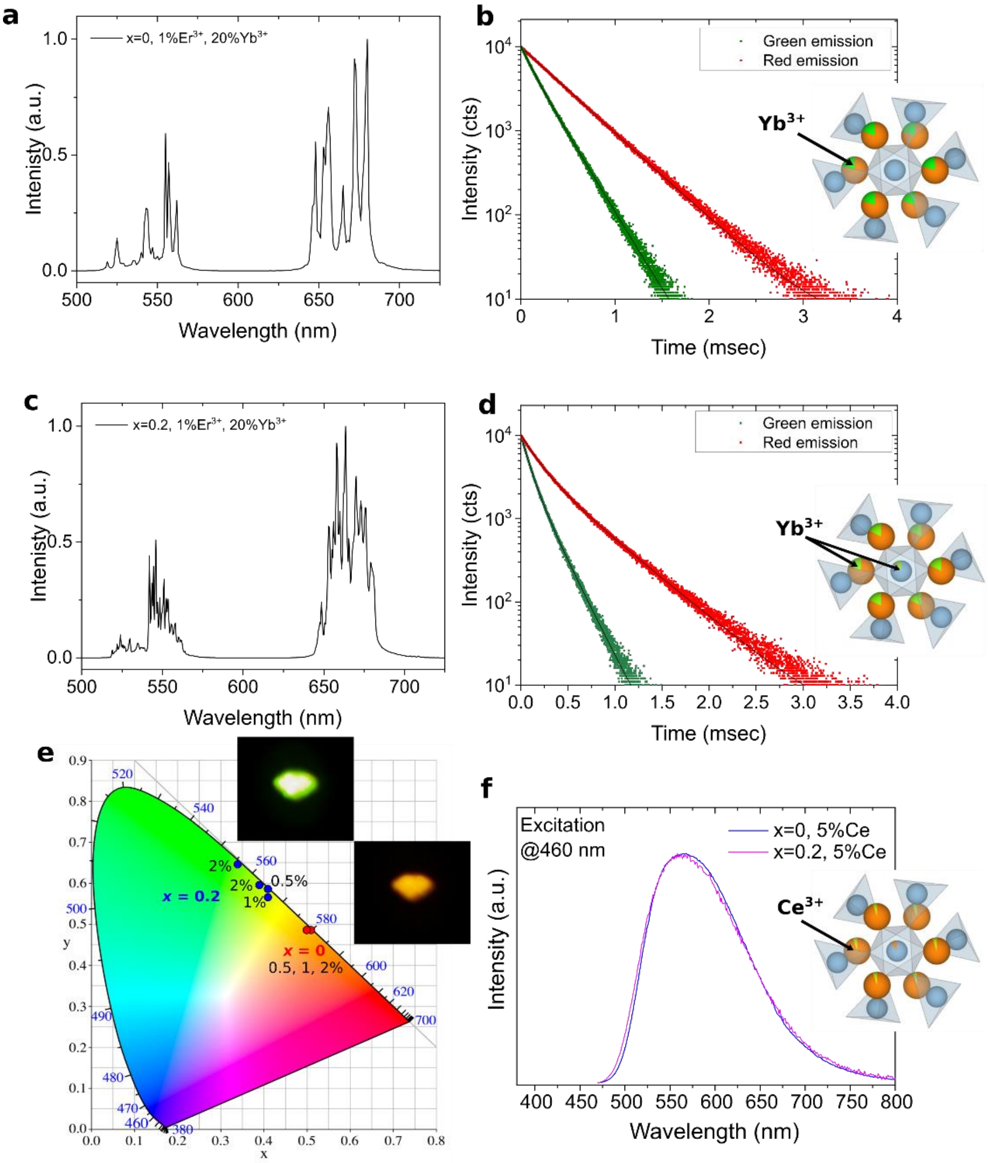

Figure 5. Influence of composition on luminescence properties of powder samples. (a,b) Normalised up-conversion emission spectra of $(Y_{0.79}Yb_{0.2}Er_{0.01})_3Al_5O_{12}$ under excitation at 980 nm, and the temporal decays of the $^4F_{9/2} \rightarrow {}^4I_{15/2}$ (red symbols) and $^4S_{3/2} \rightarrow {}^4I_{15/2}$ (green symbols) transitions, where solid lines are fits to the experimental curves. (c,d) Corresponding up-conversion emission spectra

and temporal decays of nonstoichiometric $(Y_{0.79}Yb_{0.2}Er_{0.01})_{3.2}Al_{4.8}O_{12}$. (e) CIE chromaticity coordinates showing a shift towards green emission for the nonstoichiometric samples and photographs of stoichiometric and nonstoichiometric samples taken under 980 nm laser irradiation in the dark. (f) Down-conversion emission spectra of $(Y_{0.95}Ce_{0.05})_3Al_5O_{12}$ and $(Y_{0.95}Ce_{0.05})_{3.2}Al_{4.8}O_{12}$ after 460nm excitation. The insets show structural fragments representing the Rietveld-refined locations of the dopant ions in each case.

compositions are summarised in **Table S1** along with the average decay times, $<\tau>$, of the nonstoichiometric sample. This change in the luminescence decay behaviour from exponential in $(Y_{0.78}Yb_{0.2}Er_{0.02})_3Al_5O_{12}$ to biexponential in nonstoichiometric $(Y_{0.78}Yb_{0.2}Er_{0.02})_{3.2}Al_{4.8}O_{12}$ is consistent with an increase in complexity of the material: (Yb/Er) now populate two crystallographic sites with different first-coordination spheres (AO_8 and BO_6), whilst on the local scale the AO_8 sites adopt two main configurations, by sharing a vertex with either zero or one neighbouring $(Y/Yb/Er)O_6$ sites.

Expanding the scope to other rare-earth garnets. Readily-synthesised members of the garnet aluminate family extend from $Gd_3Al_5O_{12}$ to $Lu_3Al_5O_{12}$. Y^{3+} is one of the smallest A-site cations to form this structure. To test the scope for highly nonstoichiometric garnets of other (non-YAG) compositions, the large rare-earth member $Gd_{3+x}Al_{5-x}O_{12}$ (GAG) and its corresponding gallate $Gd_{3+x}Ga_{5-x}O_{12}$ (GGG) were synthesised by the direct crystallisation method to for compositions x = 0 and 0.20. In both systems, this produced single-phase garnet structures with substantially increased unit cell volumes of +0.55% (GAG) and +0.44% (GGG) on going from x = 0 to 0.20, similar to the cell expansion exhibited by the nonstoichiometric YAG system (+0.53% on going from $Y_3Al_5O_{12}$ to $Y_{3.2}Al_{4.8}O_{12}$), indicating the formation of highly nonstoichiometric $Gd_{3.2}Al_{4.8}O_{12}$ (**Figure 6** and **Table S2**) and $Gd_{3.2}Ga_{4.8}O_{12}$ (**Figure S8** and **Table S3**). The existence of these compounds implies that highly nonstoichiometric compositions should be obtainable across the full range of functional aluminate $RE_3Al_5O_{12}$ and gallate $RE_3Ga_5O_{12}$ garnets. It is possible that such systems with $r(RE^{3+}) >> r(Y^{3+})$ will be more amenable than YAG to the arrangement of large RE^{3+} dopants such as Ce^{3+} or Nd^{3+} over two cation sublattices, whilst small rare-earth materials could be more amenable to high non-stoichiometry values, with optical materials such as the scintillator material $Lu_3Al_5O_{12}$ (LuAG)[37] or the persistent luminescent host $Y_3Al_2Ga_3O_{12}$ (YAGG)[38] as enticing targets. Future synthesis of such materials may not be limited to glass- and direct-crystallisation methods: solution or solvothermal techniques are already widely used to synthesise YAG derivatives at moderate temperatures, and it is plausible that these could facilitate synthesis and scale-up of new nonstoichiometric derivatives.

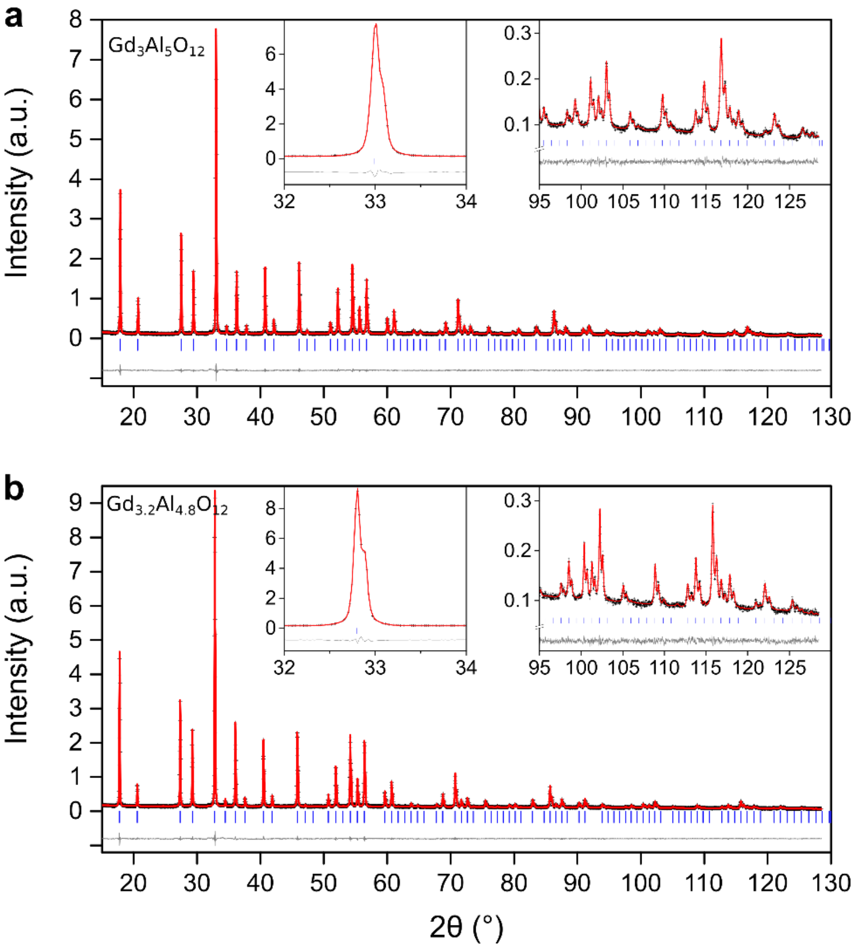

Figure 6. Lattice expansion of highly nonstoichiometric gadolinium aluminium garnet $Gd_{3+x}Al_{5-x}O_{12}$ (x = 0, 0.20), observed by PXRD (Cu K$\alpha_{1,2}$). (a, b) Le Bail fits to $Gd_3Al_5O_{12}$ and $Gd_{3.2}Al_{4.8}O_{12}$, yielding a refined unit cell volume expansion of +0.55% on going from x = 0 to 0.20, similar to that exhibited by the equivalent YAG system $Y_{3.2}Al_{4.8}O_{12}$ (+0.53%). Insets show fits to the most-intense peak (420) and the high-angle region $2\theta > 95°$. Black points = y_{obs}, red line = y_{calc}, grey line = y_{obs}- y_{calc}, blue ticks = allowed reflections. See **Table S2** for fitted parameters.

Conclusions

Non-equilibrium synthesis methods, exemplified here by the use of glass-crystallisation and direct-crystallisation of undercooled melts, offer a way to isolate a new family of highly nonstoichiometric

YAG compounds $Y_{3+x}Al_{5-x}O_{12}$ as bulk ceramics over an unprecedented compositional range $0 \leq x \leq 0.40$. The garnet structure accommodates this excess Y^{3+} by replacement of up to 20% of the octahedrally-coordinated Al^{3+} cations at the 16*a* sites. This provides a way to distribute significant concentrations of rare-earth dopants over two crystallographic sites in YAG, at the same time lifting the equivalence of the A sites by creating different nearest-neighbour configurations locally, and hence to influence the luminescence emission properties. This is demonstrated here by the use of Yb^{3+}/Er^{3+} up-conversion phosphors in a highly nonstoichiometric YAG matrix $Y_{3.2}Al_{4.8}O_{12}$, which changes the emitted colour from dominantly red to dominantly green emission. In contrast, Ce^{3+} down-conversion emission is hardly affected by nonstoichiometry in this system, because the larger ionic radius of Ce^{3+} constrains it to the *A* sublattice of the host structure. Highly nonstoichiometric compositions are accessible in other garnet-type aluminates and gallates with larger rare-earth cations, as demonstrated by the synthesis of garnet-type $Gd_{3.2}Al_{4.8}O_{12}$ and $Gd_{3.2}Ga_{4.8}O_{12}$, covering a range of current commercially exploited optical materials. The use of nonstoichiometry to control dopant distribution in such materials may offer routes to new luminescent or persistent luminescent materials with tunable emission colours, and may also yield materials with other properties such as scintillation or frustrated magnetism.

Methods

Synthesis All reactions were prepared from mixtures of high purity starting reagents Y_2O_3 (99.9%), Al_2O_3 (99.999%), CeO_2 (99.99%), Er_2O_3 (99.99%), Yb_2O_3 (99.9%), Gd_2O_3 (99.99%) and Ga_2O_3 (99.998%), all supplied by Strem Chemicals. The mixtures were ground under ethanol in an agate mortar, dried by gentle heating in air (~100°C), and pelletised with a uniaxial press. The resulting pellets were broken into fragments of <100mg. Individual pellet fragments were loaded into the nozzle of an aerodynamic levitator system and melted by a pair of CO_2 lasers (10.6 µm) using either argon or oxygen gas jets to levitate the melts. The aerodynamic stability of the levitating melt was monitored by a camera to verify the absence of contact with the nozzle, and the temperature was monitored with an optical pyrometer. The melted samples were cooled rapidly from pyrometer read-out temperatures of 2200-2300°C by switching off the lasers. Note that all temperatures quoted in the text are direct read-outs from the pyrometer; using the same apparatus, measurement of the melting point of $Y_3Al_5O_{12}$ on cooling under near-equilibrium conditions produced a value of 1840°C (**Figure S9**), somewhat lower than typical experimentally-determined values of ~1940°C,[39] implying a systematic under-estimate of ~100°C.

X-ray Diffraction Ambient temperature laboratory PXRD was carried out using a Bruker D8 Advance diffractometer (Cu Kα radiation, LynxEye detector) in Bragg-Brentano geometry with finely ground sample powders deposited on a low background silicon wafer from an ethanol mull. In-situ variable temperature X-ray diffraction (VT-PXRD) used a Bruker D8 Advance diffractometer (Cu Kα radiation, Vantec detector) equipped with an Anton Paar HTK16 furnace. Samples were deposited on to a platinum ribbon heating element from an ethanol mull, and the experiments were run under vacuum conditions to preserve the platinum heating element. Measurements were performed on heating from ambient temperature to 1600 °C, with intervals of 100 °C (in the range ambient-900 °C) and 50 °C (in the range 900-1600 °C). High-resolution synchrotron X- ray powder diffraction (SXRD) data were collected using the high-flux 11BM diffractometer operating at ~ 30 keV at the Advanced Photon Source (Argonne National Laboratory, U. S. A.). Sample powders were prepared by crushing a single bead for each composition, and were loaded under air into Kapton capillaries with an inner diameter of 0.8 mm and sealed with modelling clay. Data were recorded at room temperature in the range $0.5 \leq 2\theta \leq 50°$ with a 0.001° step size and an incident wavelength of 0.457806 Å. The data were analysed by Rietveld refinement using TOPAS Academic (v.6).

Scanning electron microscopy and microprobe analysis For both SEM imaging and microprobe compositional analyses, sample beads were embedded in epoxy resin, polished to create a flat surface, and carbon coated (thickness 15–20 nm) under vacuum. Microstructural analysis was carried out with a IT800SHL JEOL scanning electron microscope (FEG SEM) equipped with a SSD Ultim Max

100mm^2 detector (EDS Oxford system). High-precision elemental analyses were performed with a Cameca SX Five electron microprobe (EMP) at the joint BRGM–CNRS facility at Orléans. Analyses were carried out under an acceleration voltage of 15 kV, a sample current of 10 nA, a focused beam of 1 µm and a counting time of 10 s for Y and Al elements on each spot (30 spots per sample). A stoichiometric $Y_3Al_5O_{12}$ sample was used as a standard.

Transmission electron microscopy Selected area electron diffraction (SAED), high resolution transmission electron microscopy (HRTEM) imaging, atomic-resolution scanning transmission electron microscopy – high angle annular dark field (STEM-HAADF) micrographs and energy dispersive X-ray spectroscopy (EDS) elemental mapping were performed on a JEOL ARM200F (JEOL Ltd.) Cold FEG (Field Emission Gun) transmission electron microscope operating at 200kV, equipped with a double spherical aberration corrector and fitted with a JEOL SDD CENTURIO EDS system and a GIF Quantum. The cation arrangements were imaged at the atomic scale by STEM-EDS elemental mapping and in STEM-HAADF imaging mode with a 68-174.5 mrad inner-outer collection angles. The probe size used was 0.13nm and 0.1nm respectively. The thickness of the samples was estimated using electron energy loss spectroscopy (EELS). The samples were first prepared from single beads by mechanical polishing with a tripod and inlaid diamond discs, to reach a thickness of 40µm. Thin foils of 8 - 15 nm thickness were then obtained by argon ion milling (Gatan PIPS), by gradually reducing the incident beam voltage from 5 keV to 100 eV to remove beam-induced amorphisation.

NMR Measurements were carried out using Bruker Advanced III spectrometers operating at magnetic fields of 7.0 and 9.4 T, corresponding to ^{89}Y Larmor frequencies of 14.71 and 19.61 MHz, respectively. The ^{89}Y spectra were recorded using the EASY pulse sequence to efficiently remove the baseline distortion induced acoustic probe ringing occurring at low Larmor frequencies.[40] A flip angle of 90° corresponding to a pulse duration of 28.5 µs and a recycling delay of 75 s were used to avoid saturation effects. The spinning frequency was set to 5 kHz and 3 runs of 1152 transients were co-added leading to a total acquisition time of 3 days. To reduce the otherwise intractable ^{89}Y relaxation times, we used samples doped with 0.1mol% Gd^{3+}.[41] Homogenous doping levels of 0.1 mol% Gd^{3+} were achieved by first preparing 1mol%-doped reaction mixtures with Gd_2O_3 (99.99%, Strem Chemicals), then diluting them with non-doped material, prior to the final synthesis step via ADL melt-quenching (direct crystallisation). All Gd-doped samples were checked for phase purity by PXRD prior to NMR measurement.

^{27}Al NMR experiments were performed at a magnetic field of 17.6 T (^{27}Al Larmor frequency of 195.45 MHz). ^{27}Al MAS spectra were recorded at spinning frequencies of 60 kHz ($x = 0, 0.1, 0.25, 0.3, 0.4$) and 30 kHz ($x = 0.2$) using 1.3 and 2.5 mm probeheads, respectively. The ^{27}Al longitudinal relaxation times were measured to ~40s. Quantitative MAS spectra were obtained using a $\pi/18$ flip angle corresponding to a pulse duration of 0.5 µs and a recycle delay of 60s. 768 (x = 0, 0.1, 0.25, 0.3, 0.4) and 4196 transients (x = 0.2) were co-added.

EXAFS X-ray absorption fine structure experiments at the Y K-edge (17 038 eV) were performed at the DIFFABS beamline at the SOLEIL synchrotron (Gif-sur-Yvette, France). All samples were crushed to a fine powder, diluted with BN powder and compacted uniaxially to provide pellets of thickness ~250 µm and diameter 12 mm. The final beam size at the sample position was 300 µm (H) × 250 µm (V). The incident beam energy was calibrated using an yttrium foil. The experiments were performed in transmission mode, with the incident and transmitted intensities measured with two ionisation chambers operating with a nitrogen flux at atmospheric pressure as absorbing gas. The absorption coefficient was recorded by scanning from 17.0 – 17.985 keV with energy steps from 1 – 3 eV depending on the energy region, for acquisition times of 1s/point compatible with reasonable measurement times (~20 minutes/scan). To ensure a good signal-to-noise ratio, four energy scans were summed for each sample.

Luminescence Upconversion emission spectra of the Yb/Er doped samples were measured using a FLS1000 photoluminescence spectrometer (Edinburgh Instruments) equipped with a 2 W 980 nm laser as the excitation source. Fluorescence lifetimes were obtained by measuring the fluorescence decay curves using an extended range pulse width control box installed in the same instrument, which allows pulsing the 980 nm laser. The dependence of peak intensity of the green and red upconversion luminescence was recorded by changing the pump power of the 980 nm laser using an iris filter. All measurements were performed at room temperature. Ce^{3+} emission spectra of the Ce^{3+}-doped samples were recorded using the same equipment and a xenon lamp as the excitation source.

Calculations Theoretical structural models were based upon a single $Y_3Al_5O_{12}$ unit cell (1 x 1 x 1) in space group *P*1 with 160 independent atoms ($Y_{24}Al_{40}O_{96}$). Nonstoichiometric models with x = 0.125, 0.25 and 0.375 (formula $Y_3[Al_{2-x}Y_x]^{VI}[Al_3]^{IV}O_{12}$) were constructed by substitution of 1, 2 or 3 of the 16 AlO_6 sites by YO_6. Lattice parameters were fixed to Rietveld-refined values. For the models with multiple possible configurations (*i.e.* x = 0.25 and 0.375), Supercell[42] was used to identify and merge those that are symmetrically equivalent, leaving only five unique configurations for x = 0.25, and nine for x = 0.375 (see **Figures S6** and **S7**). All configurations were then relaxed by plane wave based DFT calculations with periodic boundary conditions performed using Castep.[43,44] An energy cut-off of 600 eV was used for the plane-wave basis set expansion and the Brillouin zone was sampled using a Monkhorst-Pack grid spacing of 0.04 Å^{-1}. These computational parameters were used for both geometry optimisation and calculation of ^{89}Y and ^{27}Al NMR parameters. The PAW[45,46]and GIPAW[47] algorithms were respectively used for computing the electric field gradient (EFG) and NMR chemical-shielding tensors. Expected NMR parameters were calculated from either an individual configuration (x = 0, 0.125) or from an ensemble of configurations weighted by their multiplicities (x = 0.25, 0.375). From the same weighted ensembles, theoretical EXAFS spectra were calculated for the yttrium K-edge using FEFF8[48] (see **Supporting Information Section E**).

Crystallographic information files may be obtained from CCDC/FIZ Karlsruhe via Access Structures (https://www.ccdc.cam.ac.uk/structures/), using the CSD numbers tabulated in the Supporting Information.

Acknowledgements

Financial support was provided by the ANR-18-CE08-0012 PERSIST and ANR-20-CE08-0007 CAPRE projects of the French National Research Agency and the CNRS, the I+D+I Grants RTI2018-094426-B-I00 funded by MCIN/AEI/10.13039/501100011033 and by “ERDF A way of making Europe”. PhD studentships for WC and XF were financed by the Chinese Scholarship Council (project numbers 201808450100 and 202008450026). Use of the Advanced Photon Source at Argonne National Laboratory was supported by the U. S. Department of Energy, Office of Science, Office of Basic Energy Sciences, under Contract No. DE-AC02-06CH11357. EXAFS beamtime was provided by the SOLEIL synchrotron (Gif-sur-Yvette, France) under project 99210047. This project has benefited from the microscopy facilities of the Platform MACLE-CVL which was co-funded by the European Union and Centre-Val de Loire Region (FEDER). We thank Marina Licheron and Vincent Sarou-Kanian (CEMHTI, Orléans) for assistance with cooling curve recordings; Sandra Ory (CEMHTI, Orléans) for DSC measurements; Aurélien Canizarès (CEMHTI, Orléans) for assistance with Raman measurements; Louis Hennet (ICMN, Orléans), Dominique Thiaudière and Philippe Joly (Synchrotron SOLEIL, Gif-sur-Yvette) for EXAFS data collection; and Marie-Pierre Chauvat and Pierre Ruterana (CIMAP, Caen) for TEM sample preparation by argon ion milling.

References

1. Ye, S., Xiao, F., Pan, Y. X., Ma, Y. Y. & Zhang, Q. Y. Phosphors in phosphor-converted white light-emitting diodes: Recent advances in materials, techniques and properties. *Materials Science and Engineering R: Reports* **71**, 1–34 (2010).
2. Nikl, M. & Yoshikawa, A. Recent R&D Trends in Inorganic Single-Crystal Scintillator Materials for Radiation Detection. *Adv. Opt. Mater.* **3**, 463–481 (2015).
3. Geusic, J. E., Marcos, H. M. & Van Uitert, L. G. Laser oscillations in Nd-doped yttrium aluminum, yttrium gallium and gadolinium garnets. *Appl. Phys. Lett.* **4**, 182–184 (1964).
4. Ueda, J., Kuroishi, K. & Tanabe, S. Bright persistent ceramic phosphors of Ce^{3+}-Cr^{3+}-codoped garnet able to store by blue light. *Appl. Phys. Lett.* **104**, 101904 (2014).
5. Arroyo, E., Torres Herrero, B., de la Fuente, J. M., Ocaña, M. & Becerro, A. I. Highly uniform $Y_3Al_2Ga_3O_{12}$-based nanophosphors for persistent luminescence bioimaging in the visible and NIR regions. *Inorg. Chem. Front.* **9**, 2454–2461 (2022).
6. Geller, S., Espinosa, G. P., Fullmer, L. D. & Crandall, P. B. Thermal expansion of some garnets. *Mater. Res. Bull.* **7**, 1219–1224 (1972).
7. Ashurov, M. K., Voronko, Y., Osiko, V. V., Sobol, A. A. & Timoshechkin, M. I. Spectroscopic study of stoichiometry deviation in crystals with garnet structure. *Phys. Status Solidi* **42**, 101–110 (1977).
8. Zorenko, Y. *et al.* Exciton and antisite defect-related luminescence in $Lu_3Al_5O_{12}$ and $Y_3Al_5O_{12}$ garnets. *phys. stat. sol.* **244**, 2180–2189 (2007).
9. Milanese, C., Buscaglia, V., Maglia, F. & Anselmi-Tamburini, U. Disorder and Nonstoichiometry in Synthetic Garnets $A_3B_5O_{12}$ (A = Y, Lu - La, B = Al, Fe, Ga). A Simulation Study. *Chem. Mater.* **16**, 1232–1239 (2004).
10. Liu, B., Gu, M., Liu, X., Huang, S. & Ni, C. Formation energies of antisite defects in $Y_3Al_5O_{12}$: A first-principles study. *Appl. Phys. Lett* **94**, 33504 (2009).
11. Patel, A. P. *et al.* Mechanisms of nonstoichiometry in $Y_3Al_5O_{12}$. *Appl. Phys. Lett.* **93**, 191902 (2008).
12. Sang, Y. *et al.* Yttrium aluminum garnet nanoparticles with low antisite defects studied with neutron and X-ray diffraction. *J. Solid State Chem.* **192**, 366–370 (2012).
13. Zhu, L. L. *et al.* Preparation and characterization of nonstoichiometric yttrium aluminum garnet (YAG) with antisite defects as a potential scintillator. *IEEE Trans. Nucl. Sci.* **61**, 312–315 (2014).
14. Cantarano, A. *et al.* Drastic Ce^{3+} Insertion Enhancement in YAG Garnet Nanocrystals Through a Solvothermal Route. *Front. Mater.* **8**, 768087 (2021).
15. Allix, M. *et al.* Highly Transparent $BaAl_4O_7$ Polycrystalline Ceramic Obtained by Full Crystallization from Glass. *Adv. Mater.* **24**, 5570–5575 (2012).
16. Xu, J. *et al.* Interstitial Oxide Ion Migration Mechanism in Aluminate Melilite $La_{1+x}Ca_{1-x}Al_3O_{7+0.5x}$ Ceramics Synthesized by Glass Crystallization. *ACS Appl. Energy Mater.* **2**, 2878–2888 (2019).
17. Fan, J. *et al.* $La_2Ga_3O_{7.5}$: A metastable ternary melilite with a super-excess of interstitial oxide ions synthesized by direct crystallization of the melt. *Chem. Mater.* **32**, 9016–9025 (2020).

18. Genevois, C. *et al.* Emergence of A-Site Cation Order in the Small Rare-Earth Melilites $SrREGa_3O_7$ (RE = Dy–Lu, Y). *Inorg. Chem.* **60**, 12339–12354 (2021).

19. Weber, J. K. R., Abadie, J. G., Hixson, A. D., Nordine, P. C. & Jerman, G. A. Glass Formation and Polyamorphism in Rare-Earth Oxide–Aluminum Oxide Compositions. *J. Am. Ceram. Soc.* **83**, 1868–1872 (2000).

20. He, G., Mei, L., Wang, L., Liu, G. & Li, J. Synthesis and luminescence properties of nano-/microstructured $Y_3Al_5O_{12}$:Ce^{3+} microspheres by controlled glass crystallization. *Cryst. Growth Des.* **11**, 5355–5361 (2011).

21. Michálková, M. *et al.* Viscous flow spark plasma sintering of glass microspheres with YAG composition and high tendency to crystallization. *J. Eur. Ceram. Soc.* **41**, 1537–1542 (2021).

22. Ikesue, A., Kinoshita, T., Kamata, K. & Yoshida, K. Fabrication and Optical Properties of High-Performance Polycrystalline Nd:YAG Ceramics for Solid-State Lasers. *J. Am. Ceram. Soc.* **78**, 1033–1040 (1995).

23. Benmore, C. J. & Weber, J. K. R. Aerodynamic levitation, supercooled liquids and glass formation. *Adv. Phys. X* **2**, 717–736 (2017).

24. Ma, X. *et al.* Pressureless glass crystallization of transparent yttrium aluminum garnet-based nanoceramics. *Nat. Commun.* **9**, 1175 (2018).

25. Gervais, M., Le Floch, S., Gautier, N., Massiot, D. & Coutures, J. P. Crystallization of $Y_3Al_5O_{12}$ garnet from deep undercooled melt Effect of the Al-Ga substitution. *Mater. Sci. Eng. B* **45**, 108–113 (1997).

26. Nagashio, K., Sasaki, J. & Kuribayashi, K. Phase Selection in Undercooled $Y_3Al_5O_{12}$ Melt. *Mater. Trans.* **45**, 2723–2727 (2004).

27. Skinner, L. B., Barnes, A. C., Salmon, P. S. & Crichton, W. A. Phase separation, crystallization and polyamorphism in the Y_2O_3-Al_2O_3 system. *J. Phys. Condens. Matter* **20**, 205103–205112 (2008).

28. Wilding, M. C., Wilson, M., Benmore, C. J., Weber, J. K. R. & McMillan, P. F. Structural changes in supercooled Al_2O_3-Y_2O_3 liquids. *Phys. Chem. Chem. Phys.* **15**, 8589–8605 (2013).

29. George, N. C., Denault, K. A. & Seshadri, R. Phosphors for solid-state white lighting. *Annual Review of Materials Research* **43**, 481–501 (2013).

30. Brede, R. *et al.* Green up-conversion laser emission in Er-doped crystals at room temperature. *Appl. Phys. Lett.* **63**, 2030–2031 (1993).

31. Liu, M., Wang, S. W., Zhang, J., An, L. Q. & Chen, L. D. Dominant red emission ($^4F_{9/2}\rightarrow{}^4I_{15/2}$) via upconversion in YAG ($Y_3Al_5O_{12}$):Yb^{3+},Er^{3+} nanopowders. *Opt. Mater.* **29**, 1352–1357 (2007).

32. Garskaite, E., Lindgren, M., Einarsrud, M. A. & Grande, T. Luminescent properties of rare earth (Er, Yb) doped yttrium aluminium garnet thin films and bulk samples synthesised by an aqueous sol-gel technique. *J. Eur. Ceram. Soc.* **30**, 1707–1715 (2010).

33. Desirena, H. *et al.* Photoluminescence characterization of porous YAG: Yb^{3+}–Er^{3+} nanoparticles. *J. Lumin.* **153**, 21–28 (2014).

34. Hostaša, J. *et al.* Polycrystalline Yb^{3+}-Er^{3+}-co-doped YAG: Fabrication, TEM-EDX characterization, spectroscopic properties, and comparison with the single crystal. *J. Mater. Res.* **29**, 2288–2296 (2014).

35. Chen, X. *et al.* Fabrication and spectroscopic properties of Yb/Er:YAG and Yb, Er:YAG

transparent ceramics by co-precipitation synthesis route. *J. Lumin.* **188**, 533–540 (2017).

36. Zhou, J. *et al.* Upconversion luminescence of high content Er-doped YAG transparent ceramics. *Ceram. Int.* **36**, 193–197 (2010).

37. Nikl, M. *et al.* Development of LuAG-based scintillator crystals - A review. *Prog. Cryst. Growth Charact. Mater.* **59**, 47–72 (2013).

38. Ueda, J., Dorenbos, P., Bos, A. J. J., Kuroishi, K. & Tanabe, S. Control of electron transfer between Ce^{3+} and Cr^{3+} in the $Y_3Al_{5-x}Ga_xO12$ host via conduction band engineering. *J. Mater. Chem. C* **3**, 5642–5651 (2015).

39. Caslavsky, J. L. & Viechnicki, D. J. Melting behaviour and metastability of yttrium aluminium garnet (YAG) and $YAlO_3$ determined by optical differential thermal analysis. *J. Mater. Sci. 1980 157* **15**, 1709–1718 (1980).

40. Jaeger, C. & Hemmann, F. EASY: A simple tool for simultaneously removing background, deadtime and acoustic ringing in quantitative NMR spectroscopy - Part I: Basic principle and applications. *Solid State Nucl. Magn. Reson.* **57**–**58**, 22–28 (2014).

41. Aime, S. *et al.* Insights into the use of paramagnetic Gd(III) complexes in MR-molecular imaging investigations. *J. Magn. Reson. Imaging* **16**, 394–406 (2002).

42. Okhotnikov, K., Charpentier, T. & Cadars, S. Supercell program: a combinatorial structure-generation approach for the local-level modeling of atomic substitutions and partial occupancies in crystals. *J. Cheminformatics 2016 81* **8**, 1–15 (2016).

43. Clark, S. J. *et al.* First principles methods using CASTEP. *Zeitschrift fur Krist.* **220**, 567–570 (2005).

44. Segall, M. D. *et al.* First-principles simulation: ideas, illustrations and the CASTEP code. *J. Phys. Condens. Matter* **14**, 2717–2744 (2002).

45. Profeta, M., Mauri, F. & Pickard, C. J. Accurate First Principles Prediction of ^{17}O NMR Parameters in SiO_2: Assignment of the Zeolite Ferrierite Spectrum. *J. Am. Chem. Soc.* **125**, 541–548 (2003).

46. Blöchl, P. E. Projector augmented-wave method. *Phys. Rev. B* **50**, 17953 (1994).

47. Pickard, C. J. & Mauri, F. All-electron magnetic response with pseudopotentials: NMR chemical shifts. *Phys. Rev. B* **63**, 245101 (2001).

48. Ankudinov, A. L., Ravel, B., Rehr, J. J. & Conradson, S. D. Real-space multiple-scattering calculation and interpretation of x-ray-absorption near-edge structure. *Phys. Rev. B* **58**, 7565–7576 (1998).

Conflict of Interest

The authors have no conflicts of interest to declare.

Table of Contents

A family of highly nonstoichiometric YAG ceramics is isolated by advanced melt-quenching methods. In these materials, rare-earth dopants can populate two crystallographic sublattices, providing a mechanism for luminescence colour tuning that is not available to conventional stoichiometric YAGs. The concept is generalised to other garnet ceramics including GAG and GGG, opening new avenues for exploration in this important materials class.